

Zirconium-Doped Vanadium Oxide and Ammonium Linked Layered Cathode to Construct a Full-Cell Magnesium-Ion Battery: A Realization and Structural, Electrochemical Study

Divyamahalakshmi Muthuraj,^[a] Ananta Sarkar,^[a] Manas Ranjan Panda,^[a, b] Md. Adil,^[a] Archna Sagdeo,^[c, d] and Sagar Mitra^{*[a]}

More than three times higher bulk density, easy to handle in air, and high abundance on earth crust make magnesium metal a desirable element in battery application. Several efforts have been attempted to construct the rechargeable magnesium-ion battery, unfortunately none of them are successful to a limit. Here, a new generation of vanadium oxide linked with ammonium ions is considered an active cathode for magnesium ion insertion. The Zr doped-NH₄V₄O₁₀ (Zr-NVO) nanorod exhibits an initial discharge capacity of 328 mAh g⁻¹ at 40 mA g⁻¹ current density with negligible capacity fading till 150 cycles. The estimated Mg²⁺ diffusivity in such cathode is found to be in the

range of 10⁻¹¹ to 10⁻¹² cm² s⁻¹, demonstrating a pronounced Mg-ion mobility in Zr-NVO cathode. In addition, a detailed mechanistic study is performed at different states of charge using XRD, XPS and in-situ XANES analysis. In conclusion, to achieve the ultimate goal of such study, a full-cell is assembled and evaluated by coupling tin anode with magnesiated Zr-NVO cathode. The cell has been cycled for a limited number of cycles and the reason behind the limited cycling behaviour is discussed and offers us a pathway to a resolution of the problem for rechargeable magnesium-ion battery development in the near future.

1. Introduction

Non-aqueous magnesium-ion batteries can be considered as a complementary system to Li-ion technology in many applications as it provides a high volumetric capacity (3833 mAh cm⁻³), high abundance in nature and expected to be safe in comparison to other multivalent-ion batteries.^[1–7]

Nevertheless, the practical realization of the Mg-ion battery is impeded due to several reasons like lack of suitable cathode material with excellent Mg-ion mobility, absence of electrolyte system and compatible electrolyte/electrode interface. Although the size of Mg²⁺ is lesser than Li⁺, a high charge to radius ratio induces the high migration barrier for Mg-ion diffusion in the cathode compounds.^[8–10] Aurbach et al., developed the first prototype Mg-ion battery using Chevrel phase Mo₆S₈ cathode that exhibited an excellent cycling stability, but the specific capacity and cell voltage (1.1 V) were

the significant factors and resulted in a low energy density devices.^[11,12]

Vanadium oxide and the similar compounds with layered structure is predicted to provide a better room for Mg-ion diffusion with a higher cell operating voltage.^[13–15] Although the preliminary confirmation of Mg-ion intercalation into V₂O₅ exists and revealed that a strong Coulombic interaction between oxide host and intercalated Mg-ion induces a sluggish ion diffusion kinetics. A few studies have been reported on nanostructured V₂O₅ cathode material; however, limited to Mg-ion diffusivity that leads to poor electrochemical performance. Orthorhombic V₂O₅ was demonstrated to intercalate 0.5 Mg²⁺ ($x=0.5$) in its structure reversibly.^[13] On the other hand, xerogel V₂O₅ was reported to show the facile Mg-ion insertion as water molecules within the interlayer co-ordinate with the Mg-ion and screened the charge cloud.^[16]

Ammonium vanadium oxide (NVO), a new class of studies has been reported as a high rate capable cathode material for both Li and Na-ion batteries by our research group recently.^[17,18] The NVO structure consists of double vanadium oxide layers with edge and corner shared VO₆ pyramid unit, which exhibits more electronic and ionic conductivity than V₂O₅.^[19] During the synthesis of NVO, ammonium ions are intercalated between the vanadium oxide layers to increase the interlayer *d* spacing that facilitated more cation insertion. Further, intercalated ammonium ions (NH₄⁺) act as a bridge between V–O layers and hold the crystal framework. Recently, NVO cathode is subjected to Mg-ion insertion reaction, where the report showed a stable discharge capacity of 101 mAh g⁻¹ over 100 cycles.^[19] However, the detailed mechanism and kinetic study of Mg-ion intercalation in any cathode including

[a] Dr. D. Muthuraj, Dr. A. Sarkar, Dr. M. R. Panda, M. Adil, Prof. S. Mitra
Electrochemical Energy Storage laboratory
Department of Energy Science and Engineering
Indian Institute of Technology Bombay
Powai, Mumbai 400076, India
E-mail: sagar.mittra@iitb.ac.in

[b] Dr. M. R. Panda
IITB Monash Research Academy
Powai, Mumbai 400076, India

[c] Prof. A. Sagdeo
Homi Bhabha National Institute
Anushakti Nagar, Mumbai 400094, India

[d] Prof. A. Sagdeo
Synchrotrons Utilization Section
Raja Ramanna Centre for Advanced Technology
Indore 452013, India

 Supporting information for this article is available on the WWW under
<https://doi.org/10.1002/batt.202100149>

NVO cathode and its use to fabricate the full magnesium-ion battery cell are scarce in the literature.

Here, zirconium is partially doped in place of vanadium as per our earlier studies^[17] to enhance the electronic conductivity and to improve the electrochemical properties against magnesium and current cathode exhibited an excellent performance compared to the previous reports. To endorse and investigate further, the chemical diffusivity of Mg²⁺ was examined by different electrochemical techniques including cyclic voltammetry (CV), galvanostatic intermittent titration technique (GITT) and electrochemical impedance spectroscopy (EIS) and compared. A detailed Mg-ion intercalation mechanism in Zr-NVO was studied and showed that the charge storage mainly came from diffusive and surface storage properties. In the later part, an in-situ XANES, ex-situ XPS, and XRD techniques were used to study the mechanism in more depth. This report is also attempted to construct the full-cell magnesium-ion battery (MIB) using pre-magnesiated Zr-NVO cathode and tin anode and observed the failure of the cell performance after a limited cycle due to the blocking behaviour of the anode. The current study can give us a guideline to study further with this cathode make full-cell magnesium-ion battery along with a suitable anode and electrolyte in coming future.

2. Results and Discussion

Zr-NVO is prepared by a modified hydrothermal method as reported before by our group.^[17] The X-ray diffraction (XRD) pattern confirms (Figure S1a) the formation of Zr-NVO compound, a highly polycrystalline monoclinic phase (space group C12/m1) are observed and corresponding simulated lattice parameters are $a=11.572\text{ \AA}$, $b=3.602\text{ \AA}$, $c=9.538\text{ \AA}$, $\alpha=90.0$, $\beta=100.09$, and $\gamma=90.0$ respectively. FESEM image shows that the material possesses nanorod morphology and particles are homogeneously distributed throughout the material, as shown in Figure S1(b,c). The average length and width of nanorods are estimated to be 600 nm and 100 nm respectively (Figure S1d). The nanostructure is a desirable choice for solid-state Mg-ion diffusion in the host, which further benefits this cathode. The high-resolution transmission electron microscope (HRTEM) image of a single nanorod and corresponding Fast Fourier Transform (FFT) pattern is displayed in Figure S2(a and b), respectively. The lattice fringes are matched well with the (004) plane of Zr-NVO layers with the d-spacing of 0.23 nm. Furthermore, the selected area electron diffraction (SAED) pattern confirms the polycrystalline nature of the material, and the planes are indexed as (110), (200), (003) and (004), respectively. To confirm Zr doping, we have performed XPS for NVO and Zr-NVO material. The results of XPS spectra and the fitted parameters have been added in the Supporting Information (Figure S3 and Tables S1,S2). The overall XPS survey scan of NVO and Zr-NVO is shown in Figure S3(a), which displays a prominent peak for the Zr element. The zirconium spectrum of the Zr(3d) peaks (Figure S3b) at 182.254 eV and 184.621 eV corresponds to Zr(3d)_{5/2} and Zr(3d)_{3/2} of Zr⁴⁺ oxidation state, respectively which confirms the Zr doping in NVO material.

Furthermore, V(2p) spectrum (Figure S3c) shows the peak at 517.577 eV, and 524.506 eV corresponds to V 2p_{3/2} and V 2p_{1/2} of V⁵⁺ oxidation state. The peak at 516.168 eV corresponds to V⁴⁺ oxidation state which indicates the existence of both V⁵⁺ and V⁴⁺ oxidation states in Zr-NVO material. Figure S3(d,e) compares V(2p) and O(1 s) spectra of NVO and Zr-NVO material. A significant peak shift is noticed after Zr-doping on NH₄V₄O₁₀. The peak corresponds to V⁵⁺ shifts from 517.28 eV to 517.57 eV (Figure S3d), and the peak corresponds to V⁴⁺ shifts from 515.85 eV to 516.16 eV (Figure S3e), suggests that zirconium is doped on the vanadium site. Furthermore, O1s spectra also show the peak shift from 528.07 eV to 530.04 eV, which indicates the oxygen vacancy created in the material after Zr doping. Also, the quantified mole percentage of Zr, N, and V elements from XPS analysis is shown in Table S3. We estimate the mole percentage of Zr dopant in Zr-NVO material is ~1 mol%. Furthermore, EDS elemental mapping is also performed for Zr-NVO material to demonstrate the distribution of Zr dopant throughout the material, and the results are shown in Figure S4. In addition, ICP analysis is also performed on NH₄V₄O₁₀ material to confirm the percentage of zirconium doping and the results are tabulated in Table S4. From ICP analysis, the doping concentration of Zr in the vanadium site is 1.10 mole %. So, the final formulae of NVO after Zr doping is Zr_{0.01}NH₄V_{3.956}O_{9.956}.

2.1. Zr Doping-Importance

Doping creates the anionic or cationic vacancy in the lattice of material that strongly influences electrochemical performance by changing the electric field or by lattice distortion.^[20–22] Zirconium (Zr⁴⁺) can be doped in place of vanadium (V⁵⁺) and can improve the electrochemical performance of the electrode. While doping, low valence zirconium (Zr⁴⁺) can create oxygen vacancy in the host material and effectively maintain the charge neutrality.^[23,24] However, adding bigger size zirconium (86 pm) in place of vanadium ion (68 pm) can create local distortion and electronic repulsion in the host material. It increases the bond length, expands the crystal lattice, and decreases the cationic-anionic interaction, which may increase the electrochemical performance of electrode. To assess the role of Zr doping in material, the conductivity of Zr-NVO and NVO material was obtained using four-probe method in Van der Pauw configuration (Lake Shore model 8404 AC/DCHMS) and ohmic contacts were made using conducting silver paint. The electrical conductivity of Zr-NH₄V₄O₁₀ is increased to $2.7 \times 10^{-11}\text{ S cm}^{-1}$ from undoped NH₄V₄O₁₀ material ($2.9 \times 10^{-12}\text{ S cm}^{-1}$) which ultimately helps to improve the electrochemical performance of the electrode.

To investigate the electrochemical performance, the Zr-NVO material is used as a working electrode against the activated carbon (AC) and subjected to various electrochemical techniques. Figure 1(a) represents the cyclic voltammogram (CV) of Zr-NVO electrode in magnesium perchlorate [Mg-(ClO₄)₂]/acetonitrile (ACN) electrolyte at 0.01 mV s⁻¹ scan rate in a potential range of -0.6 V to 1 V vs. AC (equivalent to 1.8 V to

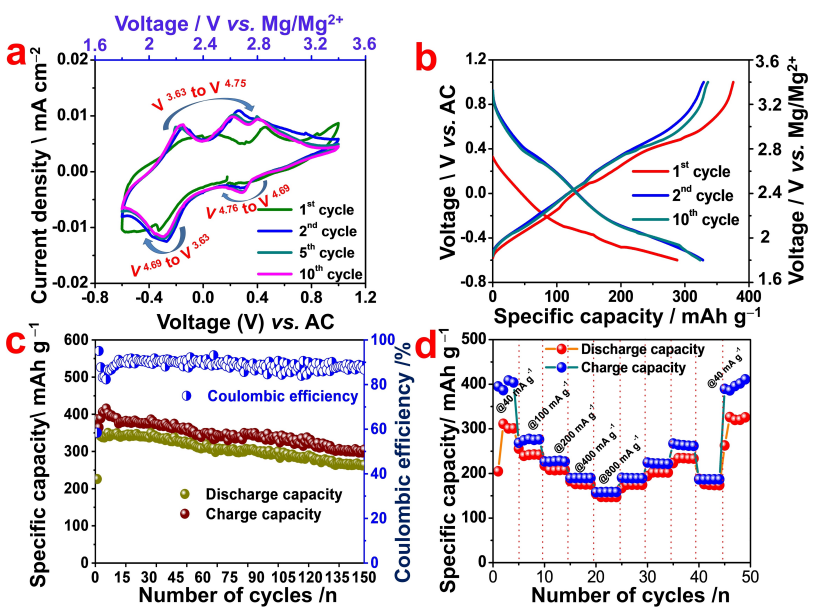


Figure 1. Electrochemical performance of Zr-NVO cathode using 0.5 M $\text{Mg}(\text{ClO}_4)_2/\text{ACN}$ electrolyte in the potential range of -0.6 V to 1 V vs. AC (1.8 V to 3.4 V vs. Mg/Mg^{2+}) in CR2032 coin cell at 20°C . The cell configuration was used here like $\text{Zr-NVO} \mid 0.5 \text{ M Mg}(\text{ClO}_4)_2/\text{ACN} \mid \text{AC}$. The active material loading is maintained to be $\sim 1.5 \text{ mg cm}^{-2}$; a) cyclic voltammograms of Zr-NVO electrode at 0.01 mVs^{-1} scan rate, b) galvanostatic discharge/charge profile of Zr-NVO cathode at 10 mA g^{-1} current density, c) cycling stability of Zr-NVO cathode at 40 mA g^{-1} current density, and d) rate performance of Zr-NVO cathode at different current density.

3.4 V vs. Mg/Mg^{2+}).^[25] The recorded electrochemical responses clearly show two sets of reduction/oxidation peaks of vanadium (III)/vanadium (V) and signify the Mg^{2+} insertion/extraction process. Two cathodic peaks are noticed at 2.11 V and 2.68 V vs. Mg^{2+}/Mg and the equivalent anodic peaks are seen at 2.24 V and 2.62 V vs. Mg^{2+}/Mg , corresponds to the reduction (V^{5+} to V^{3+}) and oxidation (V^{3+} to V^{5+}) of vanadium in the host compound. The appeared peaks are mainly due to the step-by-step transformation of Mg^{2+} insertion/extraction in the host compound. After 1st cycle, the redox peaks become more prominent. The oxidation peaks are shifted to lower potential; reduction peaks are shifted to the higher potential due to an activation process and kinetic enhancement of the electrode.^[26,27] The redox peak shifts might also be associated with the process that includes ammonium ions in $\text{Zr-NH}_4\text{V}_4\text{O}_{10}$ extraction/replacement by Mg-ion during the 1st charge process. From the 2nd cycle, the vacant ammonium-ion sites are replaced by Mg-ion to form $\text{NH}_4^+/\text{Mg}^{2+}$ combining vanadate, which serves as the cathode material in subsequent cycles. Such phenomena can be explained by the displacement-intercalation mechanism, and similar work has been observed in $\text{Mg}_x\text{V}_2\text{O}_5 \cdot n\text{H}_2\text{O}$ ^[28,29] and $\text{Ag}_0.4\text{V}_2\text{O}_5$ ^[30] for zinc-ion batteries and $\text{Ag}_{0.33}\text{V}_2\text{O}_5$ ^[31] and $\text{Cu}_{2.33}\text{V}_4\text{O}_{11}$ ^[32] materials in LIB. Furthermore, the redox peaks remain unchanged after 1st cycle, which implies good structural stability and cycling stability. It is also observed that oxidation/reduction peaks are more prominent from the 2nd cycle which suggests some structural reorganizations could occur after 1st cycle. Similar results are also observed in the previous literature.^[17] Also, the peak position and the peak shape are unchanged from 2nd cycle that confirms better reversibility of Mg^{2+} insertion/extraction process. Fresh Zr-NVO electrode exhibits mixed vanadium oxidation state (V^{5+} and

V^{4+}) and from the 2nd cycle, during the reduction process, V^{5+} and V^{4+} phase is converted to V^{3+} phase by inserting two Mg-ions stepwise into the Zr-NVO host compound. Similarly, during the oxidation process, V^{3+} and V^{4+} phase is converted to V^{5+} by extracting two Mg-ions from the host.

To understand the Mg^{2+} insertion kinetics, Voltammogram is performed at 0.1 mVs^{-1} scan rate (Figure S5a) (ten times higher scan rate than the initial CV (Figure 1a) at 0.01 mVs^{-1}). The oxidation peak separation increases from 0.57 V to 0.9 V and the reduction peak separation increases from 0.38 V to 0.63 V as the scan rate increases from 0.01 mVs^{-1} to 0.1 mVs^{-1} . This behaviour demonstrates the difficulty of solid-state Mg-ion diffusion in the cathode structure at a higher scan rate. It also indicates that the Mg^{2+} insertion process at different scan rates is not identical with respect to electrochemical reaction kinetics and the reaction voltage.^[33,34]

One more important point here is that the graphite is used as a current collector due to its excellent anticorrosive capability compared to metal current collectors.^[35] However, to demonstrate the zero capacitive contribution from graphite, blank graphite paper was used as a working electrode and subjected to CV (Figure S5b). The obtained negligible background current showcases the current contribution obtained from such cathode is entirely from Zr-NVO material alone. Figure 1(b) shows the galvanostatic charge/discharge profile of Zr-NVO cathode at 10 mA g^{-1} current density. The 1st cycle shows the discharge plateau at 2 V vs. Mg^{2+}/Mg during the discharge process. In contrast, 2nd cycle shows the two discharge plateaus at 2.8 V and 2 V . Also, the 2nd cycle delivers higher discharge capacity (328 mAh g^{-1}) than the 1st cycle (288 mAh g^{-1}) due to the absence of redox reaction at 2.8 V in the 1st cycle. Such behaviour is due to the electrode activation

in the presence of electrolyte. The 1st cycle discharge process started from OCV of the cell (~2.65 V) with the lower cut-off potential up to 1.8 V and upper cut-off potential at 3.4 V. So, the discharge plateau at 2.8 V is not utilized for 1st cycle and delivers a lesser discharge capacity than 2nd cycle. From the 2nd cycle onwards, the discharge plateau at 2.8 V can be seen, thereby giving an additional discharge capacity. A similar type of behaviour is noticed in the CV (Figure 1a) experiment as well. In brief, during the discharge process, the short plateau at 2.8 V corresponds to the reduction of V⁵⁺ to V⁴⁺ phase and the plateau at 2 V signifies the reduction of V⁴⁺ to V³⁺ phase in the Zr-NVO host compound. During the charge process, the plateau at 2.55 V and 2.85 V corresponds to phase transition of V³⁺ to V⁴⁺ and V⁴⁺ to V⁵⁺ in the host compound. Furthermore, the higher 1st cycle charge capacity (375 mAh g⁻¹) than discharge capacity (288 mAh g⁻¹) denotes the partial removal of NH₄⁺ with the extraction of Mg²⁺ which is explained by X-ray Photoelectron Spectroscopy (XPS) study (Figure 4c) in later studies.

The galvanostatic discharge/charge profile of the Zr-NVO electrode at 40 mA g⁻¹ current density is shown in Figure S5(c) and corresponding cycling stability is shown in Figure 1(c). The capacity increases after 1st cycle and provides stable capacity with further cycling. No drastic change in cycling behaviour is observed that reveals an outstanding structural stability of the material. The cell delivers 86% of the initial discharge capacity after the 150th cycle. Notably, the charge capacity in every cycle is higher than the discharge capacity and the Coulombic efficiency of Zr-NVO-AC battery is low. The main reason for high charge capacity than discharge capacity is the ammonium-ion deintercalation from the host compound during the charging process.^[19] We have confirmed this phenomenon by N1s XPS spectra on Zr-NVO electrode after 1st charge process and the results are displayed in Figure 4(e). The extra charge capacity comes from ammonium-ion extraction, which is reflected in Coulombic efficiency. By limiting the potential window to -0.6 V to 0.6 V vs. AC, the Coulombic efficiency of Zr-NVO electrode can be improved to 100%. In this work, first we allowed a few ammonium-ions to be deintercalated during the charge process, and the displaced ammonium-ion sites are utilized for Mg-ion intercalation. But the issue is that all vacant ammonium-ion sites are not occupied by Mg-ion during the intercalation process, which leads to low Coulombic efficiency.

We also feel that the trapped Mg-ion between vanadium oxide layers is responsible for the low Coulombic efficiency. Here, all Mg-ions are not extracted during the charging process which is due to the better coordination between Mg-ion and oxygen in the host compound. There is a strong Coulombic interaction between intercalated Mg-ion and oxygen in the host compound.^[20] Thus, it is difficult to extract all Mg-ion during charge process, which ultimately leads to low Coulombic efficiency. Intercalated Mg-ion between two distorted octahedra of V₂O₅ also provides structural stability with cycling. Furthermore, a stable cycling life of Zr-NVO electrode at high (0.2 A g⁻¹) current density (Figure S5d) further demonstrates structural stability and less parasitic reaction (due to less

exposure time). The power performance of Zr-NVO electrode is shown in Figure 1(d). This particular cathode delivers a discharge capacity of 300 mAh g⁻¹ at 40 mA g⁻¹, 240 mAh g⁻¹ at 0.1 A g⁻¹, 207 mAh g⁻¹ at 0.2 A g⁻¹, 175 mAh g⁻¹ at 0.4 A g⁻¹, 147 mAh g⁻¹ at 0.8 A g⁻¹ current rates, respectively. It was observed that the specific capacity decreased with an increase in current density which is usual trend due to sluggish Mg-ion diffusion and non-accessibility of solvated bulky ions into the electrode structure. The original specific capacity is retained when the current density is used at 40 mA g⁻¹. The retained reversible capacity illustrates the stability of the crystal framework at a high current density. It is noteworthy to mention here that the difference in charge-discharge capacity is prominent in the case of low current rate (40 mA g⁻¹) cycling and make us assume that the phenomenon is due to oxidation of perchlorate anion at higher voltage and gets aggravated with the higher time of exposure.^[36]

Furthermore, we have included the electrochemical performance of the undoped NVO cathode for comparison with the Zr-NVO cathode, as shown in Figure S6. Cyclic voltammetry (Figure S6a) of undoped NVO cathode is presented at 0.1 mV s⁻¹ scan rate in the potential range of -0.6 to 1 V vs. AC in Mg(ClO₄)₂/ACN electrolyte. Zr-NVO electrode shows well-defined redox peaks compare to undoped NVO, suggesting that the formation of phases was significantly depressed for undoped NVO. Similar results have been observed for Sn doped V₂O₅^[37] and Cr doped V₂O₅.^[38] Furthermore, galvanostatic charge/discharge profile (Figure S6b) and cycling performance (Figure S6c) show that undoped NVO cathode exhibits the specific discharge capacity of 125 mAh g⁻¹ after 50 cycles which is very low compared to Zr-NVO cathode. In contrast, the specific discharge capacity of the Zr-NVO cathode maintains to be 328 mAh g⁻¹ with negligible capacity fading till 150 cycles. It shows that Zr dopant has a significant role in improving the specific capacity of electrodes. Furthermore, the rate performance of the undoped NVO electrode is displayed in Figure S6d. It delivers the discharge capacity of 200 mAh g⁻¹ at 40 mA g⁻¹, 150 mAh g⁻¹ at 100 mA g⁻¹, 125 mAh g⁻¹ at 200 mA g⁻¹, 100 mAh g⁻¹ at 400 mA g⁻¹ current densities. The specific capacity values are higher for Zr doped NVO cathode than undoped NVO material, which might be due to the higher electronic conductivity of Zr-NVO material than NVO.

At this conjuncture, it is important to understand the interfacial behaviour of the electrode/electrolyte interface. An *in-situ* EIS experiment is performed, and the impedance parameters are evaluated using the Randles-circuit model. In brief, the Mg²⁺ insertion process in the Zr-NVO electrode can be categorized as follows:^[12,39] a) magnesium-ion diffusion in the electrolyte with bulk Mg-ion diffusion (R_{el}), b) charge transfer from the electrolyte to the cathode (solution to the solid-state matrix) (R_{ct}), c) Mg-ion diffusion within the electrode material, and d) transfer of electron (reduction) from current collector to Zr-NVO material. Figure 2(a-c) shows the Nyquist plot of Zr-NVO electrode at OCV, after 1st discharge (-0.6 V vs. AC) (Figure 2a-inset), 1st charge (1 V vs. AC) (Figure 2b-inset) and 2nd discharge (-0.6 V vs. AC) (Figure 2c-inset) processes respectively. The Randles circuit model (Figure 2e-inset) is

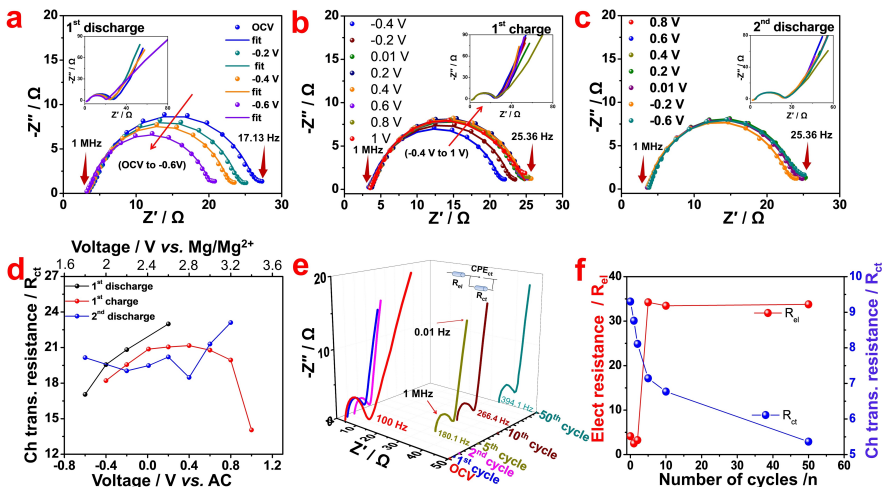


Figure 2. Interface study of Zr-NVO cathode by electrochemical impedance spectroscopy (EIS). The cell configuration was used like Zr-NVO | 0.5 M Mg(ClO₄)₂ / ACN | AC; a–c) Nyquist plot of Zr-NVO electrode during 1st discharge, 1st charge and 2nd discharge process at various potential respectively. Each inset shows the corresponding Nyquist plot in the frequency range from 1 MHz to 10 mHz frequency range at 5 mV voltage perturbation, d) variation of charge transfer resistance (R_{ct}) at different states of charge during 1st and 2nd cycle, e) EIS study of Zr-NVO electrode as a function of cycles, and f) electrolyte and charge transfer resistance (R_{el} and R_{ct}) of Zr-NVO electrode as a function of cycle numbers.

applied to the semi-circle region, and the fitted results are shown in Figure 2(d). In Randles circuit model, R_{el} , R_{ct} denotes the electrolyte resistance and charge transfer resistance, respectively. The Nyquist plots consists of medium frequency semicircle, which attributes to charge transfer resistance (R_{ct}) and inclined straight-line attributes to Warburg type impedance related to Mg-ion diffusion in the electrode material. The diameter of semi-circle decreases as Mg²⁺ is inserted (Figure 2a), which is due to decrease in R_{ct} value from 22.99 Ω to 17.05 Ω approximately.

The result supports the facile charge transfer process and easy Mg-ion intercalation in the host compound. During the charging process, the diameter of the semicircle increases as Mg²⁺ is extracted out (Figure 2b) and attained a constant value. The increase in R_{ct} value during Mg²⁺ extraction could be due to the strong Coulombic interaction between intercalated Mg-ion and oxygen in the host compound.

Furthermore, EIS was performed with an increase in cycle number from OCV to the 50th cycle (Figure 2e). The R_{ct} value (Figure 2f) was observed to be decreased from 9.29 Ω to 5.36 Ω, which explains a facile Mg-ion transfer in the host compound as the cell is cycled. Also, it is noticed that the electrolyte resistance (R_{el}) increases drastically to 34 Ω after five cycles and stays high with further cycling. The significant increment in electrolyte resistance (R_{el}) is related to the electrolyte degradation at higher potential oxidation, which is common in the case of perchlorate-based solute in the beginning and gets stabilized after a few cycles.

It was observed that the obtained specific capacity from the Zr-NVO electrode is more than the calculated theoretical capacity. Thus, it is crucial to know the extent of extra capacity that arises from the surface storage of Zr-NVO electrodes or not. To differentiate the capacitive storage from the diffusion-controlled reaction, a quantitative kinetic study of the Zr-NVO electrode is investigated. At first, the CV was performed at

different scan rates from 0.005 mVs⁻¹ to 0.1 mVs⁻¹ and displayed in Figure 3(a). The peak current is observed to be increased with an increase in scan rate (Figure S7a,d) according to the Equation (1):^[40]

$$i = av^b \quad (1)$$

The value of b decides the magnesium storage is controlled by the diffusion process ($b=0.5$) or surface storage ($b=1$).^[41] The plot between log(i) vs. log(v) gives the b value and displayed in Figure S7(b,e). The value of b is obtained for different anodic and cathodic process of peak 1 ($b_{ox}=0.81$, $b_{red}=0.64$) and peak 2 ($b_{ox}=0.7$ and $b_{red}=0.66$).

The value of b is in between 0.5 and 1, which suggests that the material shows the capacity that arises from the combination of pure diffusive behaviour and pseudo-capacitive process. The percentage of capacitive contribution at different scan rates is calculated by Dunn's equation ($i=K_1v+K_2v^{1/2}$) and demonstrated in Figure S7(c and f). The linear plot between $i/v^{1/2}$ vs. $v^{1/2}$ gives the value of K_1 (intercept) and K_2 (slope), which offers the capacitive (k_1v) as well as diffusive current ($K_2v^{1/2}$).^[40,42] The diffusive controlled capacity at different scan rates is shown in Figure 3(b). The capacitive current is estimated to be 37% (shaded region) in total current at the scan rate of 0.02 mVs⁻¹ as shown in Figure 3(c). Furthermore, to explore the diffusivity of Mg-ion is estimated by three different techniques such as CV at different scan rate, galvanostatic intermittent titration technique (GITT), and electrochemical impedance spectroscopy (EIS) study. The apparent diffusion coefficient of Mg²⁺ in the Zr-NVO electrode is estimated by the Randles-Sevcik equation [Equation (2)].^[43]

$$I_p = \frac{0.4463nFC\sqrt{DnF}}{\sqrt{RT}} \sqrt{v}, \quad (2)$$

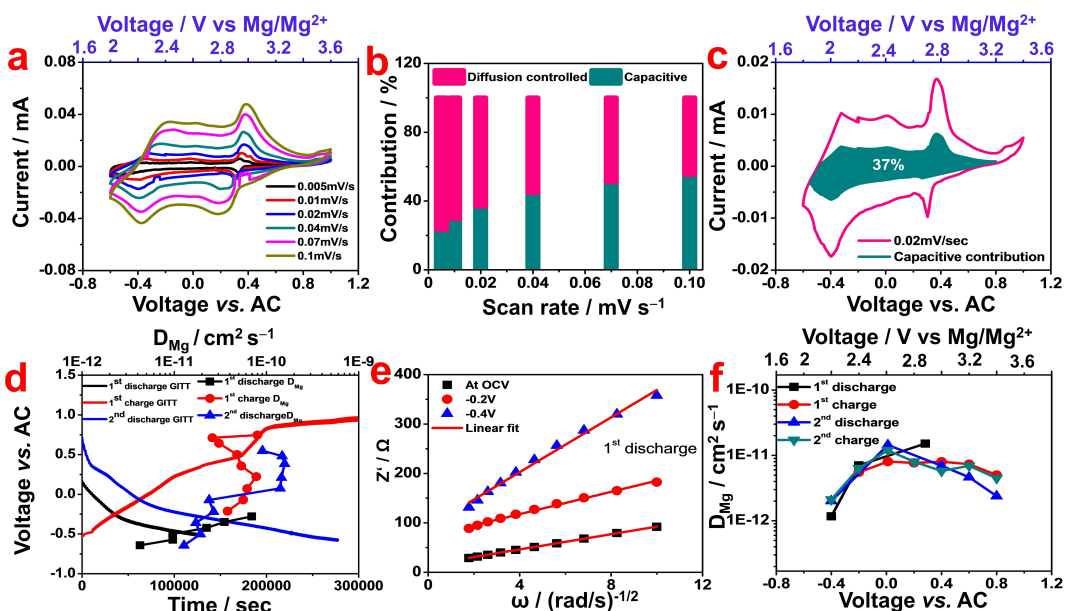


Figure 3. Capacitive contribution and Mg^{2+} diffusivity estimation in Zr-NVO electrode by CV, GITT and EIS experiments, cell configuration is Zr-NVO | 0.5 M $\text{Mg}(\text{ClO}_4)_2/\text{ACN} \mid \text{AC}$ a) cyclic voltammograms of Zr-NVO electrode at different scan rate from 0.005 mVs^{-1} to 0.1 mVs^{-1} in the potential range of -0.6 V to 1 V vs. AC (1.8 V to 3.4 V vs. Mg/Mg^{2+}) in CR2032 coin cell at 20°C , b) contribution ratio of diffusive capacity and pseudo-capacitive controlled capacity at different scan rate, c) capacitive controlled Mg^{2+} storage at scan rate of 0.02 mVs^{-1} , d) GITT curves of 1^{st} discharge, 1^{st} charge, 2^{nd} discharge and corresponding Mg-ion diffusivity at a different potential, e) linear plot between Z_{real} (Ω) and $\omega^{-1/2}$ for 1^{st} discharge at a different potential, and f) Mg-ion diffusion coefficient (D_{Mg}) calculated by EIS technique at different potential during 1^{st} discharge, 1^{st} charge, 2^{nd} discharge and 2^{nd} charge process.

where I_p is the peak Current (A), n is no of electron, F is Faraday Constant (C mol^{-1}), R is gas constant ($\text{Jmol}^{-1}\text{K}^{-1}$), T is the absolute temperature (K), v is scan rate (Vs^{-1}), D is Diffusion coefficient (cm^2s^{-1}). The plot between I_p versus scan rate (v) gives the slope value. By substituting the slope value in Equation (2), the apparent diffusion coefficient (D) of Mg^{2+} in Zr-NVO electrode is calculated, and the values are tabulated (Table S5). The diffusivity values are in the range of $10^{-11} \text{ cm}^2\text{s}^{-1}$.

In addition, GITT is a valuable technique demonstrated by Weppner et al. to calculate the diffusion coefficient of Mg^{2+} in the electrode. This method is proposed to study the variation of chemical diffusivity with the change in Mg-ion composition during the magnesiation/demagnesiation process. This technique is based on applying constant current pulse for a particular time (τ) followed by relaxation to reach a steady-state value (E_s). The cell was discharged for 15 min at constant current flux $I_0 = 0.02 \text{ mA}$ followed by 15 min relaxation steps. The potential response curve with the function of time in the potential window of 1.8 V to 3.4 V vs. Mg/Mg^{2+} is presented in Figure 3(d) for 1^{st} discharge, 1^{st} charge and 2^{nd} discharge process. Figure S8(a) shows the potential profile for single titration at $\sim 2.696 \text{ V}$ vs. Mg/Mg^{2+} during second discharge. The cell voltage variation for time τ is plotted against $\tau^{1/2}$ (Figure S8b), which displays the linear pattern with the slope of 0.000804 . Using Fick's law of diffusion, the chemical diffusion coefficient of Mg-ion in the Zr-NVO electrode is calculated [Equation (3)].^[44]

$$D_{\text{Mg}^{2+}} = \frac{4}{\pi \times \tau} \frac{m^2 V_M}{MA} \frac{\Delta E_s^2}{\Delta E_t^2}, \quad (3)$$

where m and M are the mass and molecular weight of active material and V_M is the molar volume. By substituting all these values and ΔE_s , ΔE_t values in the equation, the diffusion coefficient of Mg-ion in Zr-NVO electrode is calculated and plotted in Figure 3(d). During the first cycle discharge process, the diffusion coefficient (D) values are in the range from 10^{-10} to $10^{-12} \text{ cm}^2\text{s}^{-1}$. In the charging process, the values are $\sim 10^{-10} \text{ cm}^2\text{s}^{-1}$. In the second cycle discharge process, the D values are in the range of 10^{-10} to $10^{-11} \text{ cm}^2\text{s}^{-1}$. The estimated Mg^{2+} diffusivity values from GITT techniques are in good agreement with the result from CV measurements.

Similarly, the EIS is also a powerful tool to study Mg-ion diffusivity. The Nyquist plot for 1^{st} and 2^{nd} cycle at different potentials is presented in Figure 2(a–c) inset with the frequency range from 1 MHz to 10 mHz, which was introduced earlier. The low-frequency region in EIS corresponds to Warburg impedance which can determine Mg-ion diffusion in the electrode. The following equation is used to calculate Mg-ion diffusivity by the EIS technique [Equation (4)].^[45]

$$D_{\text{Mg}} = \frac{R^2 T^2}{2n^4 A^2 F^4 C^2 \sigma^2}, \quad (4)$$

where R is gas constant ($\text{Jmol}^{-1}\text{K}^{-1}$), T is the absolute temperature (K), n is no of electron, A is surface area of electrode, C is the concentration of Mg^{2+} in the electrode (molcm^{-3}), D is Mg^{2+} diffusivity and σ is Warburg coefficient which can be

determined from the plot between Z_{real} (Z') versus frequency ($\omega^{-1/2}$). The linear plot between Z' and $\omega^{-1/2}$ for 1st discharge (Figure 3e), 1st charge (Figure S8c), 2nd discharge (Figure S8d) and 2nd charge (Figure S8e) process is demonstrated. The slope of the linear plot gives the value of σ (Warburg coefficient). These values are substituted in Equation (4) to determine the diffusivity, and the estimated values at different potentials are shown in Figure 3(f). The D value at OCV is $1.51 \times 10^{-11} \text{ cm}^2 \text{s}^{-1}$ and substantially decreased to $1.17 \times 10^{-12} \text{ cm}^2 \text{s}^{-1}$ during 1st discharge process. The decreasing trend of D values with an increase in the composition of Mg^{2+} in the electrode might come from the phenomena of electrostatic repulsion between more Mg^{2+} in the electrode. During 2nd discharge, the apparent ion diffusivity is an increasing trend at Mg^{2+} insertion stage (initial potential) and substantially decreased while further discharged due to electrostatic repulsion. While charging, the value of D is increased and attained almost constant value in the order of $10^{-12} \text{ cm}^2 \text{s}^{-1}$ throughout the process. The obtained Mg-ion diffusivity values by the EIS technique is also consistent with the values calculated by GITT and CV. The chemical diffusivity estimated by all these three methods (CV, GITT, and EIS) are compared in Figure S8(f). The values derived from GITT are slightly higher than the values estimated from impedance spectra. Overall, the D values are consistent with methods adopted, and it is in the order of 10^{-11} to $10^{-12} \text{ cm}^2 \text{s}^{-1}$ and suggesting a good cathode material for the magnesium-ion battery.

2.2. Structural Evolution

XRD was performed on fresh Zr-NVO electrode after 1st discharge, 1st charge, 2nd discharge, 2nd charge and 20th charge processes. XRD pattern (Figure 4a,b) shows a sharp peak at 26.5° corresponds to the graphite current collector. Pristine electrode shows the monoclinic phase with a high intense peak at 8.6° corresponds to (001) plane of Zr-NVO electrode. The estimated d -spacing for the pristine electrode is 10.285 Å based on the peak at 8.6°. Other than the shift in the main peak (001), there is no new peak formation or disappearance is noticed with respect to the cycling of the Zr-NVO electrode against Mg. The zoom view of the peak at 8.6° corresponds to the (001) plane is shown in Figure 4(b). When the Zr-NVO electrode is discharged, the main peak (001) shifts to a higher angle (8.67°) and peak width was broadened which is due to the decrease in d -spacing of the V–O layer because of Mg^{2+} insertion. In the charging process, the same peak shift to a lower angle (6.69°) value. The shift in peak position explains the change in d -spacing of the electrode, could be indicative of Mg^{2+} insertion. After the 1st discharge (Mg^{2+} insertion), the layers are contracted to 10.19 Å because of the better coordination between Mg^{2+} and oxygen in the cathode.^[13,46] The distance between vanadium layers was varying based on Mg^{2+} insertion/extraction, and the change in d -spacing values are tabulated (Table S6) that indicates the layers are expanded or contracted in the z-direction [001].

After the 1st charge to the potential at 1 V vs. AC, the d -spacing value was enlarged to 13.2 Å due to the rapid extraction of Mg^{2+} . The intercalated Mg^{2+} and oxygen in

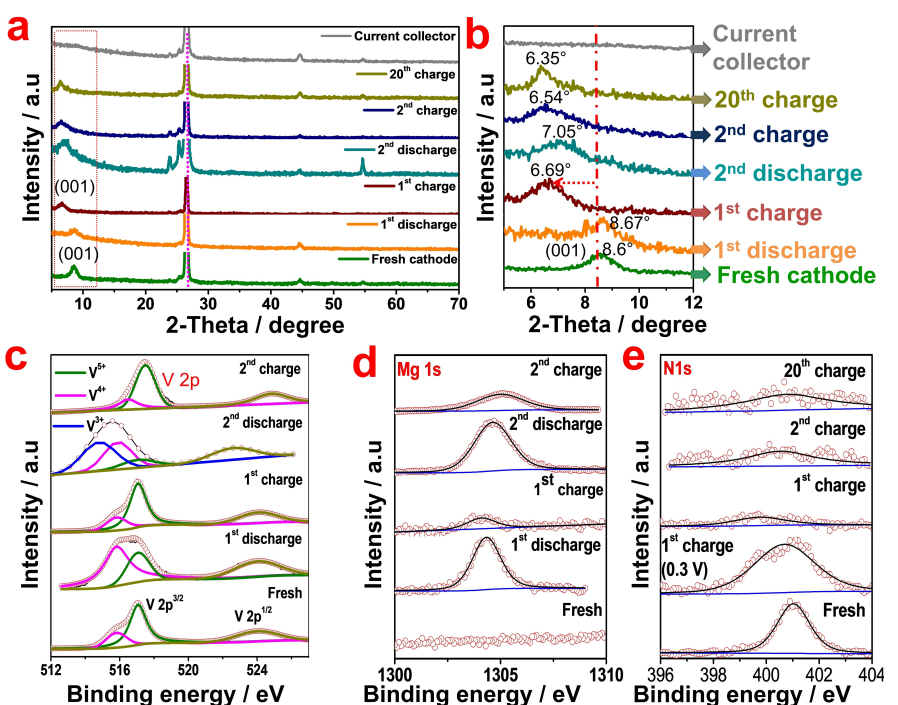


Figure 4. a) X-RD spectra for cycled Zr-NVO cathode (Zr-NVO: PVDF: Super P = 8:1:1) at various discharge and charge processes (1st, 2nd and 20th cycle). cell structure is Zr-NVO | 0.5 M $Mg(ClO_4)_2$ | ACN | AC and b) zoom view of Figure 4a in the range of 5° to 12° 2theta value, c) V(2p), d) Mg(1s), and e) N(1s) X-ray photoelectron spectra (XPS) of Zr-NVO cathode after magnesiation (1st and 2nd discharge) and de-magnesiation (1st and 2nd charge) stages.

the host compound has a strong Coulombic interaction between them. The extraction of Mg-ion leads to reduce the coordination between Mg-ion and oxygen. As explained by Mai and coworkers, the intercalated Mg-ion acts as pillar between V–O layers and provides structural stability.^[20] Thus, the extraction of Mg-ion leads to lower the coordination between Mg-ion and oxygen in the host compound, leads to expansion of vanadium oxide layers. Therefore, the d-spacing of V–O layers are noticed to be increased after Mg-ion extraction. Consequently, the increase in discharge capacity after 1st cycle comes from this phenomenon, including electrolyte oxidation. However, after 2nd discharge process, the peak was shifted to a higher angle (2-theta of 7.05°), but not entirely to its original value that again explains the contraction of Zr-NVO layers. The shift of peak to a lower angle is also observed after the 2nd and 20th cycle, respectively. The enlarged d-spacing of the electrode after every cycle is responsible for Mg-ion extraction. It is noteworthy to mention that after several expansion/contractions, V–O layers are bounded together by van-der Waals force without any structural distortion that is an indication of a good cathode.^[47]

Our interest is to estimate the extent of Mg²⁺ insertion in the Zr-NVO electrode and observe the local change in oxidation states of V. The Zr-NVO cathode was subjected to XPS study after 1st discharge, 1st charge, 2nd discharge, and 2nd charge processes, respectively. Based on V(2p), Mg(1s) and N(1s) XPS spectra, we have estimated the approximate composition of the Mg-intercalated compound during magnesiation and demagnesiation processes and the results are tabulated (Table S7).

V(2p) spectra (Figure 4c) display two split peaks correspond to the orbital V(2p)_{3/2} and V(2p)_{1/2}. V(2p)_{3/2} peak is related to the presence of V⁵⁺ (517.07 eV), and V⁴⁺ (515.82 eV) confirms the mixed oxidation states of vanadium in the virgin electrode. The ratio of V⁵⁺ to V⁴⁺ peak was estimated by deconvoluting the V(2p)_{3/2} peak and found to be 3:1. It indicates the oxidation state of vanadium in the fresh electrode is nearly V^{4.75}. After completion of 1st discharge, the peak area of V⁵⁺ is reduced simultaneously and the area under V⁴⁺ peak is increased, confirms the reduction of V⁵⁺ as Mg²⁺ is inserted. Based on this change in peak area ratio of V⁵⁺ and V⁴⁺, the valence of vanadium was approximately estimated in the following studies. The oxidation state of vanadium is estimated to be V^{4.3} after complete discharge and confirms 1.8 number of electron transfers during the 1st discharge. After charging the same electrode against Mg metal to the potential of 2.7 V vs. Mg/Mg²⁺ and 3.4 V vs. Mg/Mg²⁺, the ratios of V⁵⁺ to V⁴⁺ peak are increased to 2.67:1 and 3.22:1. It shows the oxidation state of vanadium return to its original place and approximated as V^{4.27} and V^{4.76} at 2.7 V and 3.4 V vs. Mg/Mg²⁺ respectively.

During the charging process, the increased vanadium oxidation state (V^{4.27} and V^{4.76} at 2.7 V and 3.4 V vs. Mg/Mg²⁺) re-confirms the Mg-ion extraction. After charging to the potential 2.7 V vs. Mg/Mg²⁺, the ammonium ion is released from the crystal structure (explained in N(1 s) spectra—Figure 4e). After 2nd discharge, V⁵⁺ is reduced to V⁴⁺ (515.89 eV) and V³⁺ (514.79 eV). The dominant peaks for the V⁴⁺ and V³⁺

illustrate that the more Mg-ion insertion into Zr-NVO layers. Overall, the number of Mg²⁺ inserted, the change in valence states of vanadium, the number of electrons transferred, and the corresponding expected experimental capacity were tabulated in Table S7.

Similarly, Mg(1 s) (Figure 4d) spectra display the peak at 1304 eV binding energy and confirm the Mg-ion insertion into Zr-NVO electrode. After charging, a small hump from Mg(1s) spectra shows that the Mg-ion is not entirely extracted out of Zr-NVO plane. Similarly, the signal for the nitrogen atom (Figure 4e) implies the presence of NH₄⁺ ion in the fresh and charged electrode. The peak corresponds to nitrogen is slightly deteriorated after complete charging. It indicates that the NH₄⁺ ions are slightly removed from the Zr-NVO layers at a higher potential. The N(1s) spectrum is also recorded after 2nd and 20th cycles to know the availability of NH₄⁺ ions in Zr-NVO electrode. The broad peak for the N element shows that the NH₄⁺ ions are not completely removed from the lattice. The available NH₄⁺ ions in the gallery space support the extra stability of V–O layers and prevent further structural instability. The interaction between NH₄⁺ ion and the V–O layer has a significant role in achieving cycling stability.

To infer more, V(2p) XPS spectra of Zr-NVO electrode after 20th discharge and 20th charge state is presented in Figure S9a. After 20th discharge, the vanadium reduction from V^{4.75} to V^{3.99} signifies 3 electron transfer which is equivalent to 1.5 Mg²⁺ insertions. After 20th charge, the absence of the V³⁺ peak and the increase in the V⁵⁺ to V⁴⁺ ratio signifies the reversibility of Mg²⁺ transfer. The summary of such compositional transition of Zr-NVO cathode during magnesiation and demagnesiaion process is tabulated in Table S7 (Supporting Information).

2.3. In-Situ X-ray Absorption Near Edge Structure (XANES) Study

In-situ XANES measurements were performed on the Zr-NVO electrode against Mg/Mg²⁺ using Mg(ClO₄)₂/ACN electrolyte during 1st discharge process at various discharge voltages viz. (@OCV, pristine state), 1.56 V, 1.40 V, 1.30 V, 1.15 V, 1.00 V, 0.90 V, 0.75 V, 0.42 V and 0.1 V (full discharge) respectively. The analysis is conducted in fluorescence mode at V K-edge as shown in Figure 5(a) to obtain information around the charge state and electronic structure of the absorbing vanadium atoms.^[13,42,48-51] A typical V-XANES spectrum can be classified into three parts viz. the pre-edge due to dipole forbidden 1s–3d transition, which appears because of the distortion in the octahedral symmetry due to the mixing of V-3d states with oxygen-2p states.^[52] The main absorption edge corresponds to 1s–4s monopole transition and the white line refers to the dipole 1s–4p transition.^[13,50,51,53]

Figure 5(b) demonstrates the edge step normalized vanadium K-edge XANES spectra of the Zr-NVO electrode in half-cell configuration during Mg²⁺ insertion process. The corresponding derivative of normalized vanadium K-edge XANES along with the V-metal foil (to calibrate the photon energies) and V₂O₅ (V⁵⁺, as reference), respectively are shown in Figure 5(c).

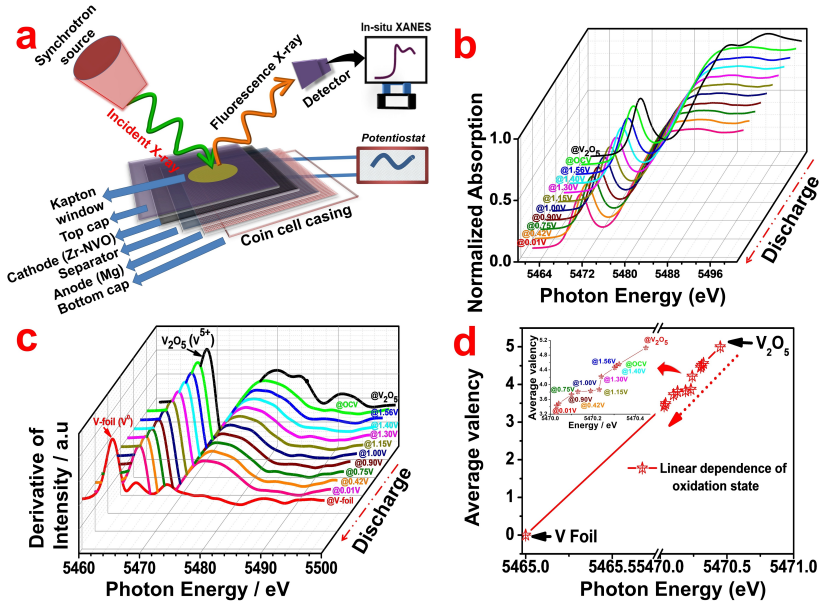


Figure 5. a) Schematic of in-situ XANES set up to test Zr-NVO electrode using coin cell configuration Zr-NVO | Mg(ClO₄)₂/ACN | Mg, b) normalized V K-edge XANES spectra of Zr-NVO electrode before cycling and during discharge process at different potential against Mg metal from OCV to 0.01 V at 20 °C, c) the first derivative of absorption data collected from XANES spectra against photon energy as a function of different state of charge, and d) average valence of vanadium in Zr-NVO electrode during the discharge process.

The vanadium K-edge spectra of the Zr-NVO electrode have shown a clear difference in the pre- and post-edge regions during the discharge process. Since XANES spectra are sensitive to the charge state and geometry of anions (oxygen) surrounding it, thus XANES spectra of the Zr-NVO electrode indicate chemical and structural modification of V-ion during magnesiation. The K-edge position (Figures 5a and S6b), obtained from the first derivative of the normalized XANES spectrum has shown a ~0.03–0.33 eV successive energy shift to lower scale for electrodes at different states of discharge voltage (@OCV to 0.01 eV), confirms the progressive vanadium reduction to varying concentrations of Mg⁺² insertion. The pre-edge spectrum of Figure 5(b) shows the precise shifting towards the lower energy during the magnesiation process. In the pristine sample electrode (i.e., @OCV), V exists in V⁵⁺ and V⁴⁺ oxidation states.^[13] The continuous decrease of the pre-edge position towards the lower energy confirmed the reduction of the average charge state of the pristine electrode V⁵⁺ and V⁴⁺ i.e. V⁵⁺ is getting converted into V⁴⁺ state due to which V⁵⁺ is getting reduced whereas V⁴⁺ is increasing.^[13,51,52]

The observed intensity of the pre-edge peak of vanadium K-edge XANES corresponds to valence, local geometry, and distortion of the (V–O) bond distances related to the octahedral symmetry of the vanadium site.^[13,51,52] There is a smooth reduction of the pre-edge peak intensity observed while increasing the concentration of Mg⁺² into the Zr-NVO host lattice (Figure 5b). The decrease in pre-edge peak intensity confirms the distortion of the structure and expansion of the vanadyl (V=O) bond distance. The above significant variation refers to the extent of distortion for the first oxygen atoms, which are further elevated, resulting in decreased local symmetry. The local structure of vanadium for the electrode at

the fully discharged state has a lower degree of local symmetry compared to the pristine state (@OCV).^[13,54] As per the above discussion, the reduction in the intensity of the pre-edge peak signifies a decrease of the distortion within the structure and the resultant increase of the basal oxygen configuration around the vanadium site as per the increase of concentration of Mg²⁺ into the Zr-NVO host structure.^[13,52,54] Further, the position of the prominent three post-edge peaks (Figure 5c) of the standard V₂O₅ XANES spectra corresponds to the V⁵⁺ characteristic features.^[13,55] During the successive discharge process of the Zr-NVO electrode, the peaks that resemble that of V₂O₅ XANES spectra seem to be less distinct, referring to the mixed oxidation state of vanadium.^[13,56]

Furthermore, Figure 5(d) shows the linear dependence of oxidation state, i.e., the variation of the oxidation state of V-ion during the magnesiation (discharge) process at the corresponding discharge potentials. Here, at the fully discharged state, the Zr-NVO electrode showed a ~0.03–0.33 eV energy shift to a lower value than the pristine state (@OCV) (Table S8). The obtained energy shift compared with the existing literature,^[13,52–59] further confirmed the reduction of V⁵⁺ and V⁴⁺ for the pristine electrode @ OCV, reduced to their corresponding lower charge states of vanadium during the discharge process, which are consistent with the XPS and obtained electrochemical results.

2.4. Post Cycling Analysis

It is essential to understand that morphological and structural changes happen while the cathode is cycled for a few cycles. To observe the change in morphology and Mg-ion distribution,

cycled electrode is subjected to SEM, EDX, and mapping analysis. SEM image (Figure S10) shows that the morphology of material was preserved after 100 cycles, but the overall particle size is reduced. After the 20th discharge, the intense peak for Mg in the EDX pattern (Figure S11a) confirms Mg-ion intercalation into the material. After the 20th charge cycle, the less intense Mg peak shows and indicates that Mg-ion is not entirely extracted from the system. Some of the Mg-ions are trapped between the vanadium oxide layers. The mapping of V, O, and N elements in the Zr-NVO electrode, after 20th discharge and after the 20th charge is shown in Figures S11(b) and S12(a,b). After the 20th discharge (Figure S12a) state, it was observed that the Mg-ion is uniformly distributed throughout the material.

In the current study, activated carbon (AC) was used as an anode to compensate the charge of Mg-ion insertion into the cathode. It is necessary to use highly porous AC with a large surface area to balance the charge of the cycling cathode. To ensure the double layer capacitance of AC, EDX is performed upon discharge and charge. Fresh activated carbon shows the peak corresponds to C and N (Figure S13a). After 1st discharge cycle (Figure S13c), the EDX pattern shows the intense peak for the Cl element, which signifies the perchlorate anions are adsorbed on AC equivalent to the Mg-ions intercalated into the Zr-NVO compound. After the 1st charge (Figure S13b), the perchlorate anions are desorbed from the carbon anode. It illustrates the reversible charge storage of AC via capacitive redox exchange behaviour. When the graphite current collector (empty) without the coating of Zr-NVO material was tested against AC, the EDX pattern shows the negligible peak corresponds to Cl and Mg, respectively. It again proves that the adsorption of perchlorate ions in AC is equivalent to the Mg-ion intercalation to compensate and charge balance in the cathode.

2.5. Full-Cell Study

Till then, we have studied in detail the cathode performance of Zr-NVO in half cell configuration. To realize the complete picture of the cathode performance in a magnesium-ion battery, we need to construct a full-cell against a known anode. Most of the conventional electrolyte solvents including ethylene carbonate, propylene carbonate, and acetonitrile used in lithium and sodium-ion battery are not compatible with Mg metal anode and form a blocking passivation layer (Figure S14a) that hinders the magnesium-ion transport. Furthermore, EDX pattern (Figure S14b) and elemental mapping (Figure S14c,d) confirm the formation of the MgO layer using acetonitrile solvent on Mg metal. Thus, magnesium-ion full-cell studies are carried out by combining Zr-NVO cathode with tin (Sn) anode.

However, Sn metal is reported as an alloy type anode material and selected here for further full-cell study.^[46] For the full-cell study, it is essential to have Mg source either in the cathode or anode side and for the same reason, the Zr-NVO cathode is electrochemically magnesiated to form a magne-

sium enriched cathode to construct the cell. By coupling the Sn anode and the magnesiated Zr-NVO cathode, a full-cell is constructed and performance parameters are demonstrated. Here, Sn nanoparticles are prepared using a chemical reduction method. XRD confirms (Figure 6a) the formation of the tin tetragonal phase with I41 space group. The size of the Sn nanoparticle is estimated to be ~50 nm (Figure S15a) from the SEM image study. Figure 6(b) shows the CV of Sn anode against magnesium metal (half-cell) in the potential range of 0.01 V to 0.8 V at 0.01 mV s⁻¹ scan rate. The CV profile displays the reduction peaks at 0.5 V and 0.25 V vs. Mg/Mg²⁺ corresponding to the formation of Mg_{Sn} and Mg₂Sn alloy compounds based on earlier reports.^[60] In the second step, the Zr-NVO electrode is subjected to discharge process to a potential up to 0.5 V against Mg metal and formed a magnesiated Zr-NVO cathode (Figure 6c). The CV profile of Zr-NVO electrode displays two reduction peaks at 1.2 V and 0.85 V vs. Mg/Mg²⁺ corresponds to the reduction of vanadium (V⁺⁵ to V⁺⁴) as Mg²⁺ is inserted in the host material.

Due to the low discharge capacity of Sn (140 mAh g⁻¹) (Figure S15b) at a current density of 10 mA g⁻¹ compares to the obtained capacity with Zr-NVO (520 mAh g⁻¹) (Figure S15c), the electrode mass loading of Sn is increased in anode side to match the cathode capacity. The mass ratio of anode and cathode was maintained as 2.5:1 to balance the charge in the cell. The full-cell is first subjected to the positive potential at the sweep rate of 0.01 mV s⁻¹ followed by a negative potential. The CV profile of full-cell (Figure 6d) shows the oxidation peak at 0.75 V and 1.3 V and the reduction peak at 1.1 V and 0.5 V. The redox behavior demonstrates the magnesiation and demagnesiation process in the cell. Galvanostatic charge/discharge profile of full-cell at 5 mA g⁻¹ current density is shown in Figure 6(e). The long discharge plateau at 1.1 V and short discharge plateau at 0.5 V signifies the magnesiation of Zr-NVO cathode and dealloying of Mg from Mg₂Sn anode. The corresponding charge plateau is obtained 0.75 V to 1 V and at 1.5 V respectively. It exactly matches to the Sn alloying with magnesium and de-magnesiation of Zr-NVO cathode. The clear distinct discharge and charge plateaus show the excellent reaction feasibility and an impressive Mg-ion reversibility in anode (Sn) (alloying) and cathode (magnesiated Zr-NVO) (intercalation). 1st cycle delivers charge and discharge capacity around 280 mAh g⁻¹ and 399 mAh g⁻¹, respectively at 5 mA g⁻¹ current density. The high discharge capacity than charge capacity is due to more polarization on the Zr-NVO cathode and improper cell balance. The 2nd cycle also shows more overpotential than the 1st cycle, and it might be a result of the increase in surface charge transfer resistance due to the inactive passivation layer formed on the Sn anode.

Full-cell charge potential (1.55 V) (Figure 6e) can be predicted by subtracting the potential for magnesiation of Sn anode (0.25 V) (Figure 6b) from the potential for demagnesiation of Zr-NVO cathode (1.8 V) (Figure S15c). Full-cell discharge potential (1 V and 0.5 V) (Figure 6e) comes from magnesiation of Zr-NVO cathode (1.2 V) (Figure S15c) and demagnesiation Mg₂Sn anode. Furthermore, galvanostatic charge/discharge performance of a full-cell is conducted at 10 mA g⁻¹ current

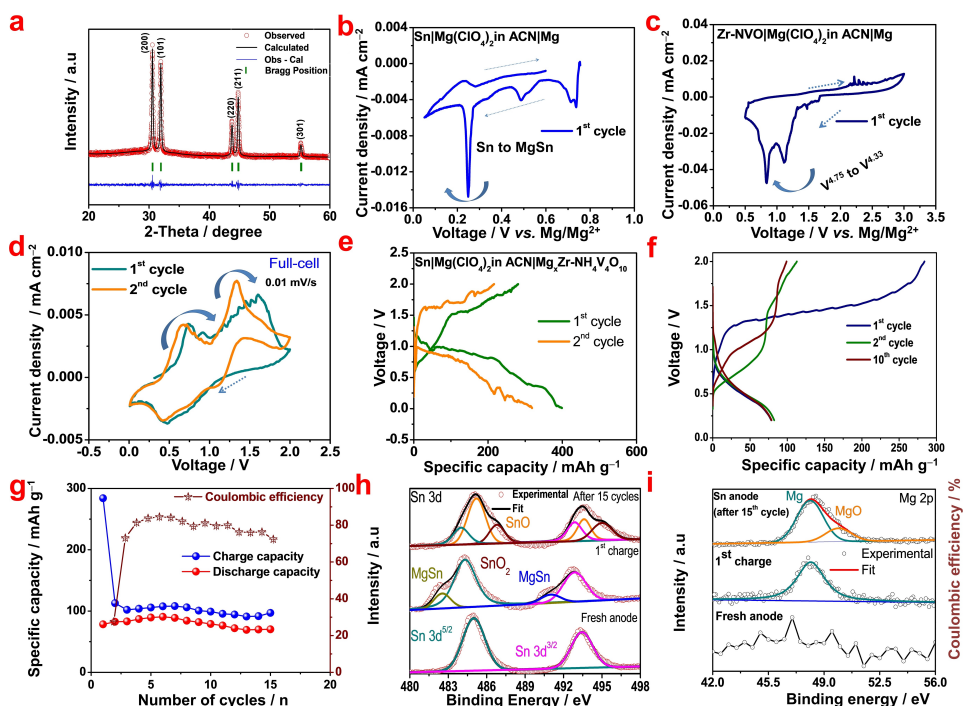


Figure 6. Full-cell study using tin anode and pre-magnesiated $\text{Zr-NH}_4\text{V}_4\text{O}_{10}$ cathode with $\text{Mg}(\text{ClO}_4)_2$ in acetonitrile a) XRD of synthesized Sn nanoparticle, b) CV of tin anode against Mg/Mg^{2+} in half-cell configuration at a scan rate of 0.01 mVs^{-1} , c) CV of Zr-NVO cathode against Mg/Mg^{2+} in half-cell configuration at a scan rate of 0.01 mVs^{-1} , d) CV of full-cell at (anode-tin, cathode-magnesiated Zr-NVO) at a scan rate of 0.01 mVs^{-1} and at a temperature of 20°C , e) galvanostatic charge/discharge profile of full-cell in the potential range of 0.01 V to 2 V at a current density of 5 mA g^{-1} , f) full-cell performance of Sn anode and magnesiated Zr-NVO cathode at 10 mA g^{-1} current density in the potential range of 0.01 V to 2 V , g) cycling stability of full-cell at 10 mA g^{-1} current density, and h) Sn(3d), and i) Mg(2p) XPS spectra of tin anode after the 1st and 15 complete cycles.

density and corresponding cell cycling stability is shown in Figure 6(f,g). The cell displays a constant charge capacity of 100 mAh g^{-1} for 15 cycles. It exhibits 80% Coulombic efficiency. This observation encourages more research on the development of MIB full-cell consist of magnesiated Zr-NVO cathode and Sn anode.

To understand the anode passivation behaviour in the current study, the XPS is performed on the fresh Sn anode after 1st cycled anode and the 15th cycled anode, respectively. The fresh Sn anode (Figure 6h) shows the peak at 484.98 eV , and 493.44 eV corresponds to $\text{Sn } 3d^{5/2}$ and $\text{Sn } 3d^{3/2}$. After the 1st cycle, the peak at 484.98 eV and 493.44 eV reveals the incomplete reaction of Sn alloying. Interestingly, the cell failure observed after the 15th cycle is mainly due to the interfacial blocking phenomena on the Sn anode. Surface analysis is performed on a cycled anode electrode (15 cycles) to understand the interfacial reaction. After the complete 15 cycles, the Sn (3d) XPS spectra (Figure 6h) shows the peak corresponds to formation of SnO (485.2 eV , 493.62 eV) and SnO_2 (486.89 eV , 495.13 eV). Similarly, the magnesium element is also investigated to understand the change in the ionic state of magnesium. The Mg (2p) XPS spectra (Figure 6i) show the peak corresponding to the MgO layer on Sn anode. Therefore, it is observed that the formed surface layer consists of SnO , SnO_2 and MgO components that comes from the interfacial charge transfer reaction between Sn anode and the electrolyte solvent. This surface layer completely blocks the Sn anode after a few cycles and distress the Mg-ion reversibility followed by the

capacity loss/cell failure. To confirm the surface layer formation visually, the Sn anode was subjected to FEG-SEM analysis (Figure S16). After the 1st discharge (Figure S16a,b), the particle size is increased which is due to volume expansion problems and usual for any alloy reactions. After the 15 cycles (Figure S16c,d), the passivation layer is formed on Sn anode surface and it is prominent from the micrographs. Although Sn is known for their outstanding alloying reaction with magnesium, the unwanted side reaction of Sn with conventional electrolyte solvent along with several other factors may prevent their cycling life in our current study.

The presented results given us a lesson that it is a universal challenge to construct a magnesium full-cell without prior knowledge and availability of compatible electrolyte that can run for a long cycling life. We believe that by controlling the interfacial reaction at the anode side and selecting a suitable and compatible anode and electrolyte solvent, we can improve the current cell performance and our research group is currently working in such direction.

3. Conclusions

A relatively new class of cathode based on vanadium oxide layered cathode has been introduced to study the magnesium ion battery electrochemistry. A pre-intercalated ammonium ion in zirconium doped vanadium oxide as a cathode material showed an excellent cathode behaviour against magnesium

and delivered a stable discharge capacity of $\sim 300 \text{ mAh g}^{-1}$ for 150 cycles at 40 mA g^{-1} current density. Various electrochemical techniques are utilized including cyclic voltammetry at different scan rates, galvanostatic intermittent titration technique and electrochemical impedance spectroscopy study to estimate the apparent Mg^{2+} diffusivity values and estimated to be in the order of $10^{-11} \text{ cm}^2 \text{ s}^{-1}$. The magnesium ion insertion and de-insertion processes are looked at by the ex-situ XRD, ex-situ XPS, and in-situ XANES. The number of magnesium ions intercalated in host compound are estimated by X-ray photoelectron spectroscopy and in-situ X-ray absorption near edge structure study, which gives the standard proof for Mg^{2+} insertion. Furthermore, a full-cell of magnesium ion battery was demonstrated by coupling with magnesiated Zr-NVO cathode with Sn alloy anode and the cell was performed well till 15 cycles. An explicit limitation of cycle life performance was observed due to inactive surface film formation on the anode side, and the reason behind the cell failure was also investigated in detail. The observation is crucial and gives us a lesson that we need to work further on electrolyte composition and suitable anode to realize a practical magnesium ion battery prototype.

Experimental Section

Materials

Vanadium Oxide (V_2O_5) (Sigma-Aldrich, 99.5%), Oxalic acid ($\text{C}_2\text{H}_2\text{O}_4$) (Merck), Ammonium hydroxide solution (NH_4OH) (Merck, 30%), Zirconium Hydroxide ($\text{Zr}(\text{OH})_4$) (Sigma-Aldrich, 97%), Hydrochloric acid (HCl) (Vetec), Activated charcoal (AC), Magnesium metal (Alfa Aesar), Sodium borohydride (NaBH_4) (Sigma-Aldrich, 99.9%), polyvinylpyrrolidone (PVP) (Aldrich), tin chloride (SnCl_2) (Merck, 98%), Diethylene glycol (DEG) (Sigma-Aldrich, 99%).

Synthesis of Zr doped ammonium vanadium oxide

Zr doped ammonium vanadium oxide (Zr-NVO) is synthesized following our previous report using the hydrothermal method.^[17] In detail, Vanadium oxide is added into the ammonium hydroxide solution (10 mL) and allowed to stir. The solution colour is changed from yellow to white. Then, 70 mL of 0.1 M oxalic acid solution was added to the mixture and allowed to stir for half an hour. Zirconium hydroxide is added to the above mixture in the molar ratio of 1: 30 (Zr: V). The pH of the mixture was maintained at three by adding HCl. Then the mixed solution is heated in an autoclave at 190°C for 5 hours. After the desired heating, the solution is allowed to centrifuge; the product is collected after washing with deionized (DI) water and dried at 60°C in Oven.

Synthesis of tin nanoparticle (Sn)

Sn nanoparticle is prepared via the chemical reduction method.^[61] In detail, 0.4741 g of SnCl_2 is dissolved in 8 ml DEG to form the precursor solution. 0.015 g of PVP is dissolved in 2 ml of DEG solution. Sodium borohydride is used as a reducing agent. The precursor solution is added dropwise into the mixed solution of sodium borohydride and PVP. The solution is stirred at high speed for 1 hour to complete the reaction. After thorough stirring, Sn

nano particles are allowed to settle, and the settled powder is dried under vacuum.

Electrochemical magnesiation of Zr-NVO

To prepare magnesium-containing cathode (Mg source in cathode side) for full cell assembly, Zr-NVO is magnesiated electrochemically against Magnesium using 0.5 M $\text{Mg}(\text{ClO}_4)_2$ in acetonitrile (ACN) solution. Zr-NVO is discharged from OCV to 0.2 V against Mg to form magnesiated Zr-NVO cathode. This electrochemically magnesiated cathode as it is in the discharged state, is utilized for full cell construction in MIB.

Material characterization

The morphology and microstructure of active material are analyzed by Field Emission Gun-Scanning Electron Microscope (FEG-SEM) (Carl Zeiss, Ultra 55) and Transmission Electron Microscope (TEM) (Jeol 2100F). X-Ray Diffraction technique (XRD) (Rigaku Smartlab, Cu K_α radiation ($\lambda = 1.5418 \text{ \AA}$)) was performed on fresh and cycled electrodes to analyze the change in phase of the electrode upon cycling. X-ray Photoelectron Spectroscopy (XPS) was demonstrated (AXIS SUPRA) on the Zr-NVO electrode at various discharge/charge potentials to illustrate the change in the oxidation state of the element. Inductively Coupled Plasma Atomic Emission Spectroscopy (ICP-AES) was carried out to estimate the percentage of Zr dopant in the host matrix.

In situ X-ray absorption near-edge structure spectroscopy (XANES)

In-situ XANES has been performed at angle dispersive X-ray diffraction (ADXRD) beamline (BL-12) (Indus-2 synchrotron source, 2.5 GeV, 200 mA), Raja Ramana centre for advanced technology (RRCAT), Indore, India.^[48-50,53] The beamline comprises of Si (111) based double crystal monochromator and two experimental stations, specifically, a six-circle diffractometer (Huber 5020) with a scintillation point detector and an image plate (Mar 345dtb) area detector. XANES measurement has been performed on Zr-NVO electrodes in in-situ mode at vanadium K-edge (5465 eV) by using the 2032-type electrochemical coin cell (Zr-NVO electrode against Mg/Mg^{2+} using $\text{Mg}(\text{ClO}_4)_2/\text{ACN}$ electrolyte) in half-cell configuration. The in-situ cell holding setup is designed so that a hole (cover with Kapton) is made at the Zr-NVO electrode side-surface to allow the incident X-ray to fall on the sample surface. The in situ cell holder setup details have been discussed in our earlier publication.^[53] The 2032 type coin-cell is then connected to the potentiometer, and the electrochemical reaction allows to perform in the potential window from OCV-0.01 V during the 1st discharge process. The electrochemical reaction is allowed to perform in the potential window from OCV (open circuit voltage) to 0.01 vs. Mg/Mg^{2+} in discharge mode. The XANES spectra are recorded in the fluorescence mode at the specifically applied discharge potentials. The sample absorption near V K-edge was observed in fluorescence by an energy-dispersive detector (Vortex-EX). The incident intensity is measured with the help of an ionization chamber placed before the sample. Photon energies before and after V K-edge were resolved using Si (111) double crystal monochromator. The XANES spectra are measured in the interval of 1 eV.^[42,48,49]

Cell assembly and electrochemical characterization

Zr-NVO slurry is prepared by mixing 80% Zr-NVO (active material), 10% PVDF (binder), 10% Super P (carbon) in NMP (N-Methyl-2-

Pyrrolidone) solvent. The mixed slurry is coated on a graphite paper current collector and used as a cathode against activated carbon (AC). The potential of AC is estimated to be 2.4 V vs. Mg/Mg²⁺.^[33,62,63] The active material loading is maintained to be ~1.5 mg cm⁻². The cells are assembled in a glove box using Swagelok and coin cell with H₂O<1 ppm, O₂<1 ppm. 0.5 M Mg(ClO₄)₂ in acetonitrile is used as an electrolyte.

Cyclic voltammetry (CV) and impedance data are collected using a Biologic instrument at 20°C. The galvanostatic charge/discharge performance was conducted in the potential range of -0.6 V to 1 V vs. AC (1.8 V to 3.4 V vs. Mg²⁺/Mg) using an ARBIN battery testing machine. For Mg intercalation study, an analogue system using Mg metal as an anode instead of AC. Sn slurry is prepared by mixing Sn, PVDF binder and super P in NMP solvent in 0.84:0.08:0.08 ratio. Then the prepared slurry is coated on copper foil and used as an anode. Sn is tested against Mg in 0.5 M Mg(ClO₄)₂/ACN for half-cell assembly. MIB full-cell is assembled using electrochemically magnesiated Zr-NVO as cathode and Sn as the anode in the potential range of 0.01 V to 2 V. An electrochemical impedance spectrum (EIS) was collected in the frequency range of 1 MHz to 10 mHz at different discharge/charge potentials and with cycling. The applied voltage perturbation is 5 mV. Cyclic voltammetry at different scan rate (0.005 mV/s, 0.01 mV/s, 0.02 mV/s, 0.04 mV/s, 0.07 mV/s, 0.1 mV/s) is performed in the potential range of -0.6 V to 1 V vs. AC to estimate the capacitive contribution of Zr-NVO electrode. Galvanostatic Intermittent Titration Technique (GITT) is performed at a constant current flux (0.02 mA) for 15 min followed by 15 min rest period in the potential range of -0.6 V to 1 V vs. AC (1.8 V to 3.4 V vs. Mg²⁺/Mg) to estimate Mg²⁺ diffusivity in electrode.

Acknowledgements

All battery fabrication and electrochemical tests were conducted using the facility funded by the National Centre for Photovoltaic Research and Education (NCPRE) and the Ministry of New and Renewable Energy (MNRE), Govt. of India. The authors acknowledge the characterization facility provided by the Industrial Research and Consultancy Centre (IRCC) and the Sophisticated Analytical Instrument Facility (SAIF) at IIT Bombay. M. R. P. would like to thank IITB-Monash Research Academy for the Ph.D. fellowship. The authors are thankful to Dr. Sudeep Sarkar, Garima Agarwal, and Murali Krishna for their helpful discussion during manuscript preparation. The authors are also grateful to Supriya Sau, Dr. A. K. Sinha, Abhay Bhisikar, Anuj Upadhyay, and M. N. Singh for helping to conduct the in-situ XANES experiment.

Conflict of Interest

The authors declare no conflict of interest.

Keywords: cell failure · full-cell study · magnesium-ion battery · passivation · vanadium oxide-based cathode

[1] M. M. Huie, D. C. Bock, E. S. Takeuchi, A. C. Marschilok, K. J. Takeuchi, *Coord. Chem. Rev.* **2015**, *287*, 15–27.

- [2] C. B. Bucur, T. Gregory, A. G. Oliver, J. Muldoon, *J. Phys. Chem. Lett.* **2015**, *6*, 3578–3591.
- [3] G. Sai Gautam, P. Canepa, A. Abdellahi, A. Urban, R. Malik, G. Ceder, *Chem. Mater.* **2015**, *27*, 3733–3742.
- [4] S. Wu, F. Zhang, Y. Tang, *Adv. Sci.* **2018**, *5*, 1701082.
- [5] M.-C. Lin, M. Gong, B. Lu, Y. Wu, D.-Y. Wang, M. Guan, M. Angell, C. Chen, J. Yang, B.-J. Hwang, H. Dai, *Nature* **2015**, *520*, 325–328.
- [6] M. Adil, P. K. Dutta, S. Mitra, *Chemistry Select* **2018**, *3*, 3687–3690.
- [7] A. Konarov, N. Voronina, J. H. Jo, Z. Bakenov, Y. K. Sun, S. T. Myung, *ACS Energy Lett.* **2018**, *3*, 2620–2640.
- [8] S. Okamoto, T. Ichitsubo, T. Kawaguchi, Y. Kumagai, F. Oba, S. Yagi, K. Shimokawa, N. Goto, T. Doi, E. Matsubara, *Adv. Sci.* **2015**, *2*, 1–9.
- [9] L. R. De Jesus, J. L. Andrews, A. Parija, S. Banerjee, *ACS Energy Lett.* **2018**, *3*, 915–931.
- [10] X. Sun, L. Blanc, G. M. Nolis, P. Bonnick, J. Cabana, L. F. Nazar, *Chem. Mater.* **2018**, *30*, 121–128.
- [11] S. H. Choi, J. S. Kim, S. G. Woo, W. Cho, S. Y. Choi, J. Choi, K. T. Lee, M. S. Park, Y. J. Kim, *ACS Appl. Mater. Interfaces* **2015**, *7*, 7016–7024.
- [12] P. Saha, P. H. Jampani, M. K. Datta, C. U. Okoli, A. Manivannan, P. N. Kumta, *J. Electrochem. Soc.* **2014**, *161*, A593–A598.
- [13] N. Sa, T. L. Kinnibrugh, H. Wang, G. Sai Gautam, K. W. Chapman, J. T. Vaughan, B. Key, T. T. Fister, J. W. Freeland, D. L. Proffit, P. J. Chupas, G. Ceder, J. G. Barenco, I. D. Bloom, A. K. Burrell, *Chem. Mater.* **2016**, *28*, 2962–2969.
- [14] Q. An, Y. Li, H. Deog Yoo, S. Chen, Q. Ru, L. Mai, Y. Yao, *Nano Energy* **2015**, *18*, 265–272.
- [15] R. H. Kim, J. S. Kim, H. J. Kim, W. S. Chang, D. W. Han, S. S. Lee, S. G. Doo, *J. Mater. Chem. A* **2014**, *2*, 20636–20641.
- [16] G. Sai Gautam, P. Canepa, W. D. Richards, R. Malik, G. Ceder, *Nano Lett.* **2016**, *16*, 2426–2431.
- [17] A. Sarkar, S. Sarkar, S. Mitra, *J. Mater. Chem. A* **2017**, *5*, 24929–24941.
- [18] S. Sarkar, P. S. Veluri, S. Mitra, *Electrochim. Acta* **2014**, *132*, 448–456.
- [19] E. A. Esparcia, M. S. Chae, J. D. Ocon, S. T. Hong, *Chem. Mater.* **2018**, *30*, 3690–3696.
- [20] Y. Xu, X. Deng, Q. Li, G. Zhang, F. Xiong, S. Tan, Q. Wei, J. Lu, J. Li, Q. An, L. Mai, *Chem* **2019**, *5*, 1194–1209.
- [21] F. Xiong, S. Tan, X. Yao, Q. An, L. Mai, *Mater. Today* **2021**, *45*, 169–190.
- [22] L. Wei, R. Lian, D. Wang, Y. Zhao, D. Yang, H. Zhao, Y. Wang, G. Chen, Y. Wei, *ACS Appl. Mater. Interfaces* **2021**, *13*, 30625.
- [23] A. Sarkar, S. Mitra, *J. Power Sources* **2020**, *452*, 227832.
- [24] A. Sarkar, C. V. Manohar, S. Mitra, *Nano Energy* **2020**, *70*, 104520.
- [25] M. Rastgoo-Deylam, M. S. Chae, S. T. Hong, *Chem. Mater.* **2018**, *30*, 7464–7472.
- [26] J. Wu, Q. L. Jia-Li Yan, Gang-Qin Shao, Shu-Hao Fan, Can Zhu, Yong Zhang, *Molecules* **2019**, *24*, 1893.
- [27] Z. Li, X. Mu, Z. Zhao-Karger, T. Diemant, R. J. Behm, C. Kübel, M. Fichtner, *Nat. Commun.* **2018**, *9*, 5115.
- [28] F. Ming, H. Liang, Y. Lei, S. Kandambeth, M. Eddaoudi, H. N. Alshareef, *ACS Energy Lett.* **2018**, *3*, 2602–2609.
- [29] Y. Zhang, H. Li, S. Huang, S. Fan, L. Sun, B. Tian, F. Chen, Y. Wang, Y. Shi, H. Y. Yang, *Nano-Micro Lett.* **2020**, *12*, 60.
- [30] L. Shan, Y. Yang, W. Zhang, H. Chen, G. Fang, J. Zhou, S. Liang, *Energy Storage Mater.* **2019**, *18*, 10–14.
- [31] W. Hu, X. B. Zhang, Y. L. Cheng, C. Y. Wu, F. Cao, L. M. Wang, *ChemSusChem* **2011**, *4*, 1091–1094.
- [32] M. Morcrette, P. Rozier, L. Dupont, E. Mugnier, L. Sannier, J. Galy, J. M. Tarascon, *Nat. Mater.* **2003**, *2*, 755–761.
- [33] R. Attias, M. Salama, B. Hirsch, Y. Gofer, D. Aurbach, *ChemElectroChem* **2018**, *5*, 3514–3524.
- [34] M. D. Levi, E. Lancry, H. Gizbar, Z. Lu, E. Levi, Y. Gofer, D. Aurbach, *J. Electrochem. Soc.* **2004**, *151*, 1044–1051.
- [35] Z. Zhou, N. Li, Y. Yang, H. Chen, S. Jiao, W. L. Song, D. Fang, *Adv. Energy Mater.* **2018**, *8*, 1–10.
- [36] E. R. Fadel, F. Faglioni, G. Samsonidze, N. Molinari, B. V. Merinov, W. A. Goddard, J. C. Grossman, J. P. Mailoa, B. Kozinsky, *Nat. Commun.* **2019**, *10*, 1–10.
- [37] Y. Li, J. Yao, E. Uchaker, M. Zhang, J. Tian, *J. Phys. Chem. C* **2013**, *117*, 23507–23514.
- [38] S. Y. Zhan, C. Z. Wang, K. Nikolowski, H. Ehrenberg, G. Chen, Y. J. Wei, *Solid State Ionics* **2009**, *180*, 1198–1203.
- [39] L. Wang, J. Zhao, X. He, J. Gao, J. Li, C. Wan, C. Jiang, *Int. J. Electrochem. Sci.* **2012**, *7*, 345–353.
- [40] J. Kang, Q. Su, H. Feng, P. Huang, G. Du, B. Xu, *Electrochim. Acta* **2019**, *301*, 29–38.

- [41] X. Zhao, W. Wang, Z. Hou, X. Fan, G. Wei, Y. Yu, Q. Di, Y. Liu, Z. Quan, J. Zhang, *Inorg. Chem. Front.* **2019**, *6*, 562–565.
- [42] M. Adil, A. Sarkar, A. Roy, M. R. Panda, A. Nagendra, S. Mitra, *ACS Appl. Mater. Interfaces* **2020**, *12*, 11489–11503.
- [43] Y. Xiao, Y. F. Zhu, H. R. Yao, P. F. Wang, X. D. Zhang, H. Li, X. Yang, L. Gu, Y. C. Li, T. Wang, Y. X. Yin, X. D. Guo, B. H. Zhong, Y. G. Guo, *Adv. Energy Mater.* **2019**, *9*, 1–8.
- [44] X. H. Rui, N. Ding, J. Liu, C. Li, C. H. Chen, *Electrochim. Acta* **2010**, *55*, 2384–2390.
- [45] J. Zhao, L. Wang, X. He, C. Wan, C. Jiang, *Int. J. Electrochem. Sci.* **2010**, *5*, 478–488.
- [46] S. Tepavcevic, Y. Liu, D. Zhou, B. Lai, J. Maser, X. Zuo, H. Chan, P. Král, C. S. Johnson, V. Stamenkovic, N. M. Markovic, T. Rajh, *ACS Nano* **2015**, *9*, 8194–8205.
- [47] G. Gershinsky, H. D. Yoo, Y. Gofer, D. Aurbach, *Langmuir* **2013**, *29*, 10964–10972.
- [48] M. R. Panda, R. N. Bhowmik, H. Singh, M. N. Singh, A. K. Sinha, *Mater. Res. Express* **2015**, *2*, 036101.
- [49] M. R. Panda, K. Anish Raj, A. Ghosh, A. Kumar, D. Muthuraj, S. Sau, W. Yu, Y. Zhang, A. K. Sinha, M. Weyland, Q. Bao, S. Mitra, *Nano Energy* **2019**, *64*, 103951.
- [50] S. Singh, K. Anish Raj, M. R. Panda, R. Sen, P. Johari, A. K. Sinha, S. S. Meena, S. Mitra, *ACS Appl. Mater. Interfaces* **2019**, *2*, 6584–6598.
- [51] F. De Groot, *Chem. Rev.* **2001**, *101*, 1779–1808.
- [52] M. Giorgetti, S. Passerini, W. H. Smyrl, S. Mukerjee, X. Q. Yang, J. McBreen, *J. Electrochem. Soc.* **1999**, *146*, 2387–2392.
- [53] M. R. Panda, R. Gangwar, D. Muthuraj, S. Sau, D. Pandey, A. Banerjee, A. Chakrabarti, A. Sagdeo, M. Weyland, M. Majumder, Q. Bao, S. Mitra, *Small* **2020**, *16*, 1–16.
- [54] A. N. Mansour, P. H. Smith, W. M. Baker, M. Balasubramanian, J. McBreen, *J. Electrochem. Soc.* **2003**, *150*, A403–A413.
- [55] S. Lee, T. L. Meyer, S. Park, T. Egami, H. N. Lee, *Appl. Phys. Lett.* **2014**, *105*, 223515.
- [56] R. Zimmermann, R. Claessen, F. Reinert, P. Steiner, S. Hüfner, *J. Phys. Condens. Matter* **1998**, *10*, 5697–5716.
- [57] K. Palanisamy, J. H. Um, M. Jeong, W. S. Yoon, *Sci. Rep.* **2016**, *6*, 31275.
- [58] M. Croft, D. Sills, M. Greenblatt, C. Lee, *Phys. Rev. B: Condens. Matter Phys.* **1997**, *55*, 8726–8732.
- [59] G. P. Holland, F. Huguenin, R. M. Torresi, D. A. Buttry, *J. Electrochem. Soc.* **2003**, *150*, A721–A725.
- [60] N. Singh, T. S. Arthur, C. Ling, M. Matsui, F. Mizuno, *Chem. Commun.* **2013**, *49*, 149–151.
- [61] S. S. Chee, J. H. Lee, *Electron. Mater. Lett.* **2012**, *8*, 587–593.
- [62] H. Tang, F. Xiong, Y. Jiang, C. Pei, S. Tan, W. Yang, M. Li, Q. An, L. Mai, *Nano Energy* **2019**, *58*, 347–354.
- [63] R. Attias, M. Salama, B. Hirsch, R. Pant, Y. Gofer, D. Aurbach, *ACS Energy Lett.* **2019**, *4*, 209–214.

Manuscript received: July 9, 2021

Revised manuscript received: August 8, 2021

Accepted manuscript online: August 16, 2021

Version of record online: September 22, 2021